Polymer Testing 153 (2025) 109026

Contents lists available at ScienceDirect

Polymer Testing

journal homepage: www.elsevier.com/locate/polytest

Viscoelastic interpretation of AFM nanoindentation for predicting nanoscale stiffness in soft biomaterials

Antonio Minopoli [a,b], Davide Evangelista [a,b], Matteo Marras [a,b], Giordano Perini [a,b], Valentina Palmieri [c], Marco De Spirito [a,b], Massimiliano Papi [a,b,*]

[a] Dipartimento di Neuroscienze, Università Cattolica Del Sacro Cuore, Largo Francesco Vito 1, 00168, Rome, Italy
[b] Fondazione Policlinico Universitario A. Gemelli IRCSS, 00168, Rome, Italy
[c] Istituto Dei Sistemi Complessi, Consiglio Nazionale Delle Ricerche, CNR, Via Dei Taurini 19, 00185, Rome, Italy

ARTICLE INFO

Keywords:
Atomic force microscopy
Nanoindentation
Viscoelastic polymers
Hydrogels
Standard linear solid model

ABSTRACT

Precise characterization of biomechanical properties at the micro- and nanoscale is essential for developing biomaterials for tissue engineering, regenerative medicine, and drug delivery. Traditional bulk techniques fail to capture the local mechanical heterogeneities of soft materials such as hydrogels, polymers, and biological tissues. Atomic force microscopy (AFM) nanoindentation enables high-resolution stiffness mapping under near-physiological conditions; however, the standard Hertz model assumes purely elastic behavior, overlooking the viscoelastic nature of most biological systems. This study relies on established viscoelastic models to better interpret rate-dependent mechanical responses in AFM nanoindentation experiments. Force-displacement curves were analyzed to separate elastic and viscous contributions and account for the effect of indentation speed. Experiments on four hydrogels (alginate, Cellink-RGD, GelMA, GelMA A) revealed nonlinear stiffening trends with increasing indentation rate, associated with polymer network dynamics and crosslinking density. Additional analyses on erythrocytes and zona pellucida confirmed their complex viscoelastic responses, highlighting physiological and pathological differences in cells and species-specific behavior in reproductive structures. Our approach provides a simple and effective method to predict nanoscale stiffness as a function of indentation rate, improving accuracy in nanomechanical characterization and supporting the design of advanced bioengineered constructs.

1. Introduction

The precise characterization of biomechanical properties is crucial for the development of advanced 3D bioprinted constructs for biomedical applications, including tissue engineering, regenerative medicine, and drug delivery systems [1–4]. These materials are designed to replicate the complex mechanical microenvironments of native tissues, where subtle differences in local stiffness can profoundly influence cell behavior, including adhesion, proliferation, and differentiation [5–7]. Therefore, accurate measurement of biomechanical parameters such as Young's modulus at the micro- and nanoscale is essential to ensure their functional performance.

Conventional bulk testing methods, such as uniaxial compression or rheometry, provide macroscopic information but lack the spatial resolution needed to capture local mechanical heterogeneities within soft or microstructured materials. These local variations are particularly relevant in hydrogels and polymer networks that often exhibit microscale gradients in crosslinking density, porosity, or hydration. Furthermore, bulk methods generally require larger sample volumes, which can be impractical when dealing with microscale hydrogels, thin polymer films, or tissue-engineered constructs [8].

To overcome these limitations, microscale and nanoscale techniques such as atomic force microscopy (AFM) nanoindentation [8,9], optical tweezers [10], and magnetic bead microrheometry [11] have been developed to probe local mechanical properties under near-physiological conditions. Among these, AFM nanoindentation has emerged as a robust and versatile tool, enabling high-resolution mapping of local stiffness while simultaneously acquiring topographical information [12,13]. Its precise force control and broad range of measurable forces and indentation depths make it particularly well suited for characterizing soft and biological materials [14,15].

In AFM experiments, the elastic properties of materials are

* Corresponding author. Dipartimento di Neuroscienze, Università Cattolica del Sacro Cuore, Largo Francesco Vito 1, 00168, Rome, Italy.
E-mail address: massimiliano.papi@unicatt.it (M. Papi).

https://doi.org/10.1016/j.polymertesting.2025.109026
Received 23 July 2025; Received in revised form 24 October 2025; Accepted 29 October 2025
Available online 31 October 2025

commonly evaluated by analyzing force–displacement curves using the Hertz contact model applied to the approach segment of the curve [16]. This yields an apparent Young's modulus under the assumption that the material behaves as a purely elastic, isotropic, and homogeneous solid. However, most hydrogels, polymers, and biological samples are inherently viscoelastic [17]. This viscoelasticity is evidenced by hysteresis between the approach and retraction curves, a clear dependence of the apparent modulus on indentation speed, and phenomena such as stress relaxation and creep. These factors violate the assumptions of purely elastic models and can lead to significant misinterpretation of the mechanical behavior of the samples if viscoelastic effects are not properly accounted for.

Despite growing awareness of these limitations, a standardized framework to extract the intrinsic elastic modulus from force–displacement curves is still lacking [13,18,19]. To address this gap, we propose two simple models that enable the decoupling of elastic and viscous contributions directly from standard AFM nanoindentation data. The first is based on the standard linear solid (SLS) model, which effectively captures both stress relaxation and creep, making it suitable for describing viscoelastic materials that exhibit a balance of elastic and viscous contributions. The second employs a linear Voigt model, which accounts for creep effect in materials, as it captures time-dependent strain under constant stress but does not describe stress relaxation. By applying these models, it becomes possible to correct the apparent Young's modulus derived from the Hertz analysis, thereby providing a more accurate estimation of the actual elastic modulus of viscoelastic materials.

2. Materials and methods

2.1. Viscoelastic models

Hertz contact model relies on some assumptions: (i) the investigated material is elastic, isotropic, and homogeneous, (ii) the indentation depth is negligible compared to sample dimensions, and (iii) no adhesion or friction between tip and sample. Sneddon model extended Hertz model to non-spherical tips (e.g. conical tips), assuming a homogeneously distributed stress along the material with a force following the equation:

$$F = E \cdot \frac{2\tan(\theta)}{\pi(1-\upsilon^2)} \cdot \delta^2 \tag{1}$$

where F is the indentation force, E is the Young's modulus, θ is the half-opening tip angle, υ is the Poisson's ratio, and δ is the indentation depth.

To model viscoelastic indentation, several models have been proposed but none of them accounts for shear rate indentation [20–23]. In this work, we take this variable into account by assuming initially that the material locally behaves according to two different models: (i) Kelvin-Voigt model and standard linear solid (SLS) model.

2.1.1. Kelvin-Voigt assumption

In the linear Kelvin Voigt model, the material response is modelled by a spring and a dashpot in parallel (Fig. 1(a)), so that the total stress σ follows the equation [24]:

$$\sigma(t) = E \cdot \varepsilon(t) + \eta \cdot \frac{d\varepsilon(t)}{dt} \tag{2}$$

where η is the viscosity of the material, ε is the normal strain. The second term of Eq. (2) represents the viscous resistance to the strain rate. Under the same Sneddon hypotheses for non-spherical tips, the area is quadratically proportional to δ. The resulting viscous force becomes:

$$F_{\text{visc}}(\delta) = \frac{2\tan(\theta)}{\pi(1-\upsilon^2)} \cdot \frac{\eta \cdot r}{L} \cdot \delta^2 \tag{3}$$

in which L is the maximum indentation depth and r is the indentation rate. Therefore, the total indentation force is the sum of the elastic term from Eq. (1) and the viscous term from Eq. (3).

$$F(\delta) = \frac{2\tan(\theta)}{\pi(1-\nu^2)} \left(E + \frac{\eta}{L} \cdot r\right) \cdot \delta^2 \tag{4}$$

From Eq. (4), we define the apparent Young's Modulus:

$$E_{\text{app}}(r) = E_0 + \frac{\eta}{L} r \tag{5}$$

where E_0 is the Young's Modulus for very low indentation rates. Eq. (5) provides a linear dependence of the apparent modulus as a function of strain rate, as long as (i) deformations are small (i.e. $\delta \ll R_c$ the characteristic radius of the object) and (ii) the strain field $u(z,t) \sim u(z)$ is time independent.

2.1.2. Standard linear solid assumption

A more exhaustive model that accounts for the nonlinear behavior of viscoelastic materials under specific stimulus is the SLS model, consisting of a series of dashpot and spring in parallel with another spring (Fig. 1(b)). The corresponding constitutive equation is [25]:

$$\sigma(t) = E_0 \varepsilon(t) + \sigma_M(t) \tag{6}$$

where E_0 is the stiffness of the parallel spring and σ_M is the stress experienced by the dashpot and spring in series, coming from:

$$\frac{d\varepsilon_M}{dt} = \frac{1}{E_1}\frac{d\sigma_M}{dt} + \frac{\sigma_M}{\eta} \tag{7}$$

in which E_1 is the stiffness of the spring in series. Combining Eq. (6) with Eq. (7), the constitutive equation for the SLS model is:

$$\dot{\sigma} + \frac{E_1}{\eta}\sigma(t) = (E_0 + E_1)\,\dot{\varepsilon} + \frac{E_0 E_1}{\eta}\,\varepsilon(t) \tag{8}$$

whose solutions depend on the applied stimulus (e.g., creep test or stress relaxation test). Nevertheless, these solutions do not exhibit explicit dependence on the strain rate. Some models have been proposed to extend SLS model to strain rate sensitivity [25,26]. However, they need pre-existing knowledge on creep and relaxation constants not easily deductible, and are not inherently applicable for nanoindentation characterization.

In this regard, we build upon the SLS model, analyzing two limit conditions: (i) $\tau \gg \tau_c$ in which the viscous behavior is predominant with respect to the elastic one, (ii) $\tau \ll \tau_c$ in which the solid-like behavior

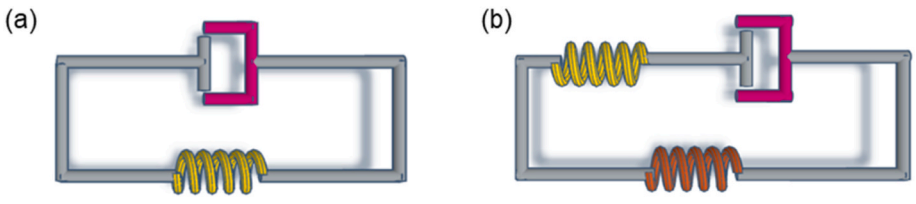

Fig. 1. Scheme of (a) Kelvin-Voigt model consisting of dashpot (red element) and spring (yellow) in parallel, and (b) SLS model consisting of a spring (orange) in parallel with a spring (yellow) and a dashpot (red) in series.

dominates over the viscous response, being τ the dashpot relaxation time of the SLS model and $\tau_c = L/r$ the characteristic relaxation time of the material. If the material is loaded much faster than it can relax, the spring fully contributes to the response ($E \sim E_0 + E_1$). In contrast, if the loading is very slow, the Maxwell branch has sufficient time to flow, and its elastic contribution vanishes ($E \sim E_0$).

Therefore, we propose a simple solution for the apparent modulus that satisfies both its asymptotical behaviors:

$$E_{app}(r) = E_0 + \frac{E_1 \cdot \eta^* \cdot r}{E_1 \cdot L + \eta^* \cdot r} \quad (9)$$

where E_0 represents ideally the intrinsic stiffness of the material, remaining even after viscous contribution is over, E_1 the transient elastic modulus, representing the time-dependent molecular chains contribution, and η^* the effective viscosity.

2.2. Constructs fabrication

GelMA, GelMA A, Cellink-RGD, and alginate were purchased from Cellink (CELLINK®, Gothenburg, Sweden). A volume of 20 μL of each gel was drop-casted in a Petri Dish. Alginate and Cellink-RGD (alginate covalently conjugated with RGD, the cell-attachment peptide sequence, and nanofibrillated cellulose) were crosslinked using a solution of $CaCl_2$ (3 % w/v) for 5 min, GelMA (gelatin methacrylated) was crosslinked using 405 nm UV light for 60 s, whereas GelMA A (a blend of GelMA and alginate) was crosslinked using sequentially both protocols. After crosslinking, all the droplets were incubated in distilled water overnight at room temperature.

2.3. Nanoindentation testing

In a standard AFM indentation experiment, a cantilever equipped with a specifically shaped tip approaches the sample surface at a controlled velocity. The cantilever indents the sample until a set maximum force is achieved, after which it retracts, detaching from the surface. During this process, the cantilever deflection and displacement are recorded and analyzed to determine the sample mechanical properties. Typically, the apparent Young's modulus can be retrieved from the force-indentation curve.

In this work, we used Nanowizard II AFM (JPK Instruments), equipped with tips (HQ:CSC37/No Al, MikroMasch) with a nominal spring constant of 0.3 N/m, tip radius of 8 nm and cone angle of 40° (Fig. 2(a)). Such a sharp tip allowed us to probe sample at the nanoscale, enabling detection of local mechanical variations with high spatial resolution. The spring constant was carefully determined by thermal calibration in distilled water before each measurement. Force curves were acquired with a 5.5 nN force limit and different indentation speeds from 0.5 μm/s to 15 μm/s with a maximum indentation depth of 5 μm keeping the samples in distilled water and in a controlled environment. A total of 64 measurements were made in a 10 μm × 10 μm square matrix per each condition.

The Young's Modulus was retrieved using JPK Data Processing software, fitting each force distance curve with Hertz-Sneddon model, assuming a Poisson ratio of 0.33, a value commonly used for hydrogels

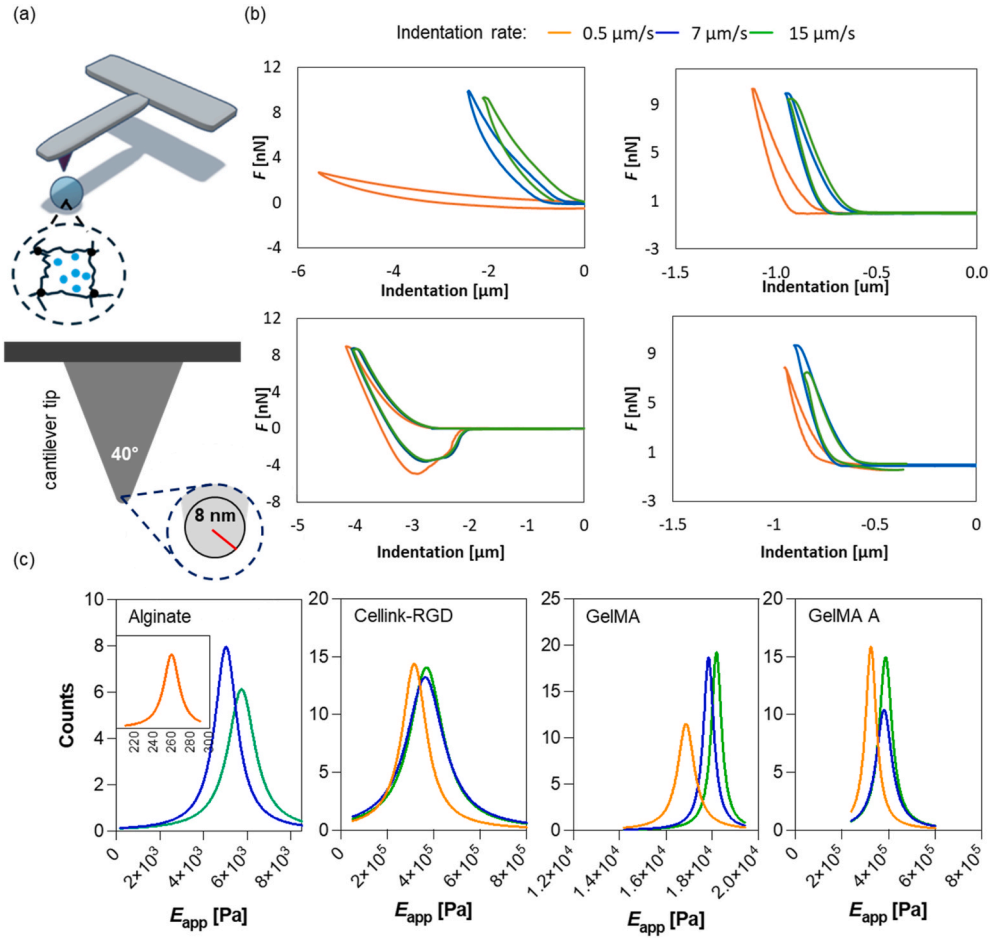

Fig. 2. (a) Sketch of AFM cantilever equipped with conical tip probing a generic hydrogel. Representative (b) force-indentation curves and (c) apparent Young's modulus distributions measured by probing alginate, Cellink-RGD, GelMA, and GelMA A constructs with a conical tip at different indentation rates. Apparent Young's modulus distributions in panel (c) were fitted using Lorentzian functions over 64 measurements.

and soft biomaterials in the literature. This assumption is consistent with previous reports on alginate- and gelatin-based hydrogels, which typically exhibit Poisson's ratios in the range of 0.2–0.4 [27–30]. For each condition, the frequency distribution is fitted with Lorentzian curve and the peak represent the values of the Young's modulus. Stiffness as a function of the indentation rate was plotted using the software GraphPad Prism 9 (GraphPad Software, San Diego, CA, USA), and the curves were fitted with a non-linear fit, with Eq. (5) and Eq. (9).

2.4. Rheology testing

Rheological measurements were carried out using a controlled-stress rheometer (MARS 60, HAAKE GmbH, Germany) equipped with a parallel plate-plate geometry (25 mm diameter, Fig. 4(j)). Hydrogel samples were prepared by extrusion into circular molds (25 mm in diameter, 1 mm thickness) and crosslinked according to the protocol described in Section 2.2. Prior to testing, samples were equilibrated at 25 °C. Amplitude sweep tests were performed at oscillation frequency 1 Hz to retrieve the linear viscoelastic region (LVR) of each formulation within a strain (γ) range of 0.01–10. Frequency sweep tests were performed in the

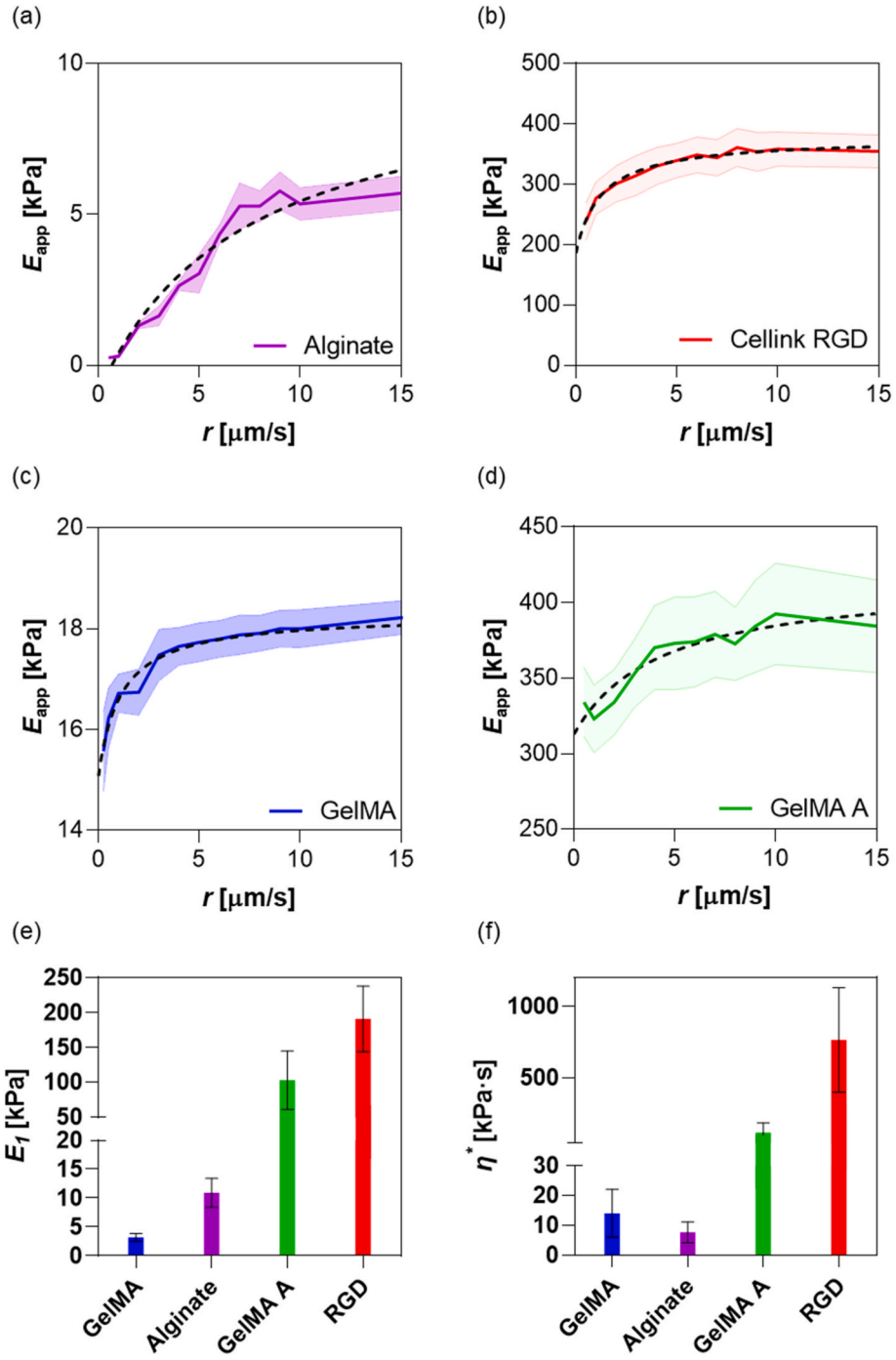

Fig. 3. Apparent Young's modulus of (a) alginate, (b) Cellink-RGD, (c) GelMA, and (d) GelMA A as a function of indentation rate. The solid lines represent the estimated values of the apparent Young's modulus over 64 measurements, whereas the shaded areas the corresponding standard deviations. The data were fitted using Eq. (9) (dashed black lines). (e) Transient elastic moduli and (f) effective viscosities of the investigated hydrogels.

range of 0.1–10 Hz under oscillatory mode at constant strain according to LVR results (alginate $\gamma = 0.005$, Cellink-RGD $\gamma = 0.01$, GelMA $\gamma = 0.01$, GelMA A $\gamma = 0.01$) to determine the viscoelastic properties of the hydrogels.

3. Results and discussion

3.1. Nanomechanics of biomedical relevant hydrogels

To evaluate the time-dependent mechanical response of the tested biomaterials, AFM nanoindentation was performed at varying indentation speeds, ranging from 0.5 μm/s to 15 μm/s. Representative force–displacement curves for each biomaterial—alginate, Cellink-RGD, GelMA, and GelMA A—are shown in Fig. 2(b). In all cases, the indentation profiles exhibit characteristic viscoelastic features, most notably hysteresis between the approach and retraction segments of the curves. For all materials tested, a clear trend emerges: hysteresis decreases with increasing indentation speeds, whereas at lower indentation speeds, viscous dissipation dominates.

To further elucidate the viscoelastic behavior of the investigated hydrogels, we analyzed the distributions of E_{app}. The apparent stiffness was calculated from the approach curve as described in Section 2.3, and the resulting distributions were fitted with Lorentzian functions to extract the peak modulus (Fig. 2(c)). The sharpness of the Lorentzian peaks suggests good mechanical homogeneity of all the samples. The Lorentzian width provides a useful indicator of mechanical heterogeneity at the microscale, which is critical for applications such as tissue engineering, where local stiffness gradients can influence cell behavior [31].

In all gels, we observed a nonlinear monotonic increase of the Young's modulus as a function of the indentation rate (Fig. 3), with an asymptotic behavior, indicating a transition from time-dependent (viscoelastic) to time-independent (elastic) mechanical response as the probing speed increases. In particular, the nonlinear increase is ascribable to different polymer dynamics: at low indentation rates, curves are steeper because the polymer network has time to rearrange under load, whereas, at higher rates, the network is probed on timescales shorter than its relaxation time (Fig. 3(a)–(d)). In addition, the parameter E_1

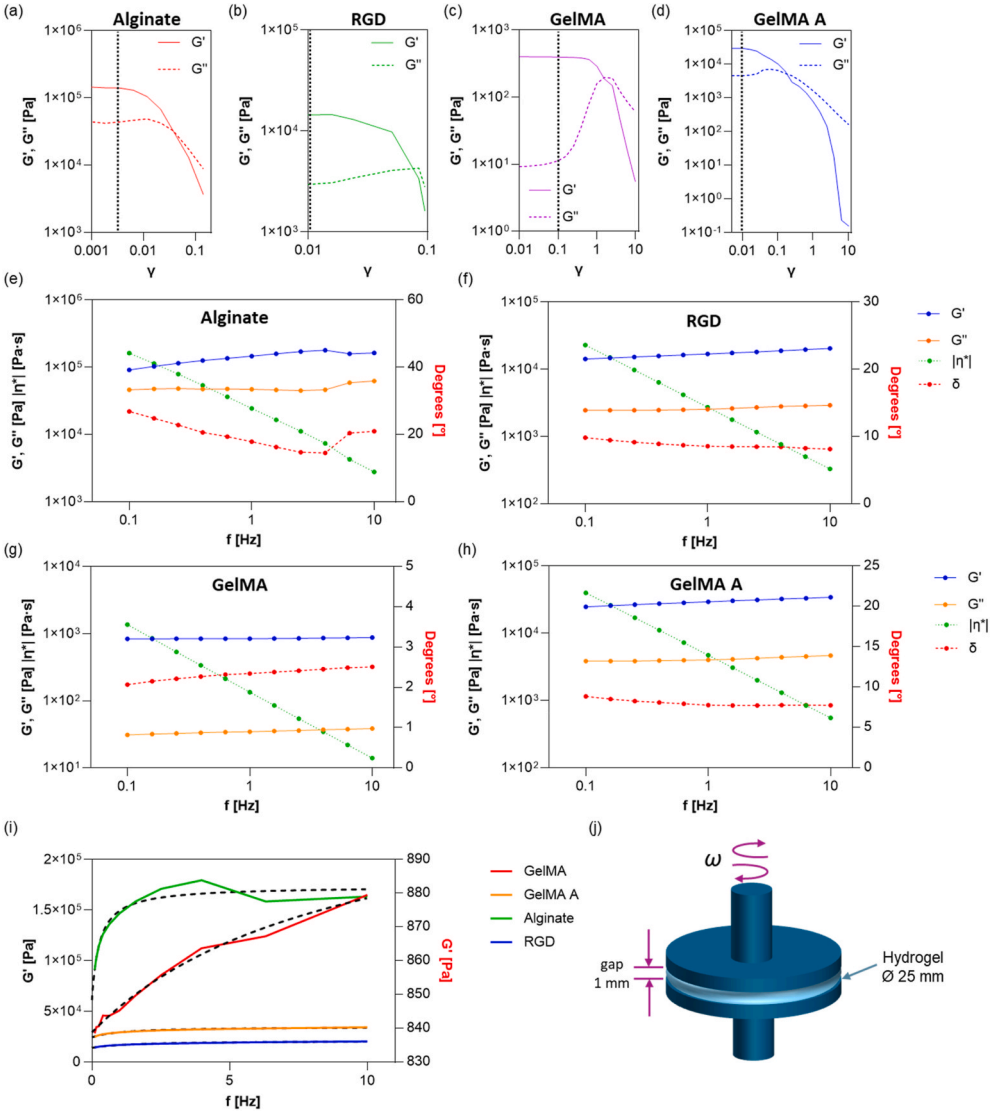

Fig. 4. Storage modulus (G') and loss modulus (G'') as a function of strain at constant frequency of 1 Hz for (a) alginate, (b) Cellink-RGD, (c) GelMA, and (d) GelMA A hydrogels. Vertical dashed lines indicate the limits of the LVR. Storage modulus (G'), loss modulus (G''), complex viscosity (η^*), and phase angle (δ) as a function of oscillation frequency at constant strain for (e) alginate, (f) Cellink-RGD, (g) GelMA, and (h) GelMA A. (i) Storage moduli fitted with SLS model (Eq. (9), dashed black lines). For clarity of comparison, data corresponding to GelMA are reported with respect to the right *y*-axis. (j) Schematic representation of the oscillatory plate–plate setup used for rheological measurements.

from Eq. (9), reflecting the magnitude of rate-dependent stiffening, varies substantially across materials. Specifically, it exhibits the lowest values in alginate and pure GelMA, and the highest in RGD and GelMA A (Fig. 3(e)), thereby highlighting how network composition and reinforcement (e.g., via nanocellulose or crosslink density) modulate viscoelastic behavior.

The mechanical behavior of alginate is explained by its structure composed of β-D-mannuronic acid (M units) and α-L-guluronic acid (G units) arranged in varying sequences along the chain [32]. Its mechanical strength arises from ionic crosslinking, so its behavior depends on G: M ratio and its topology [33]. Regarding GelMa composition, its structure is a crosslinked polymeric network via photopolymerization of methacryloyl groups grafted onto gelatin chains. The network is stabilized by both covalent (chemical) crosslinks and reversible physical interactions (e.g., hydrogen bonding, chain entanglements), especially when interpenetrating polymer networks or additional physical crosslinkers are present [34]. GelMa exhibits both a micro arrangement of the polymer network and a fluid flow (poroelasticity) with the porous structure, more pronounced in softer gels with larger pores [35]. The addition of nanocellulose and RGD sequence in alginate (Cellink-RGD) leads to a 17-fold stiffening (Fig. 3(e)) while maintaining the same nonlinear shape, due to the reduction of the free volume between alginate polymer chains and physical interpenetration of nanocellulose [36]. Counterintuitively, we observed a 34-fold increase of stiffness even in GelMA A (Fig. 3(e)) in which alginate should weaken the GelMA structure. This is due to the physical and chemical crosslinkings that caused a synergistic effect on both macromolecular chains [37].

Nanoindentation-derived effective viscosity values for the four hydrogels reveal clear trends that correlate with stiffness and network structure. Notably, alginate and pure GelMA (gelatin methacryloyl) show the lowest effective viscosities, whereas Cellink-RGD and GelMA A exhibit the highest (Fig. 3(f)). This means that the reinforced or more highly crosslinked networks in Cellink-RGD and GelMA A not only are stiffer but also dissipate more energy through viscous mechanisms than the softer alginate or GelMA. In fact, a positive correlation between apparent stiffness and effective viscosity was observed: as the hydrogels stiffen, their effective viscosity increases. Mechanistically, higher viscosity in these hydrogels reflects greater viscoelastic energy dissipation (e.g., from polymer chain motion, bond break/reform events, and internal friction [38]) during indentation. This makes sense because a densely crosslinked or reinforced polymer network resists rapid deformation – effectively "freezing" the structure at high loading rates – and in doing so, it converts more input energy into dissipative losses (viscous drag) rather than purely elastic storage. In contrast, a more loosely crosslinked hydrogel like alginate can rearrange its polymer chains more readily under stress, leading to lower viscosity and a more purely elastic response at the nanoscale [39,40].

3.2. Macrorheology characterization

Preliminary amplitude sweep tests were performed at a constant frequency of 1 Hz to assess the viscoelastic response of the hydrogels (Fig. 4(a)–(d)). For each formulation, the highest strain value within the LVR was identified and selected for subsequent frequency sweep measurements. In the frequency sweep tests, all hydrogel formulations exhibited the typical viscoelastic behavior characterized by a monotonic increase in both the storage (G') and loss (G'') moduli as a function of frequency (Fig. 4(e)–(h)). The storage moduli of alginate, Cellink-RGD and GelMA A were accurately fitted using the SLS model, which effectively captured the transition from a viscous-dominated regime at low frequencies (<1 Hz) to an elastic-dominated regime at higher frequencies. For these hydrogels, the phase angle (δ) decreased with increasing frequency, indicating reduced viscous dissipation and the predominance of elastic network dynamics (Fig. 4(e),(f),(h)). In contrast, GelMA exhibits only a gradual increase in both G' and G'' across the entire frequency range, resulting in an almost frequency-independent phase angle. These findings confirm that the selected viscoelastic model reliably describe the rheological behavior of the hydrogels under oscillatory loading, highlighting frequency-dependent stiffening associated with polymer chain dynamics and crosslinking density. It should be emphasized that these rheological measurements were performed at the macroscopic scale. Although differences in absolute values arise from distinct experimental conditions, a consistent trend was observed across all hydrogels (Fig. 3(a)–(d) and Fig. 4(i)): stiffness increased with rising probing frequency or oscillation rate, reflecting common viscoelastic mechanisms. This consistency across scales reinforces the robustness of the proposed viscoelastic modeling approach in capturing the intrinsic polymer network dynamics of the investigated gels.

3.3. Biomechanical characterization of ex-vivo biological tissues

3.3.1. Healthy and pathological erythrocytes

We have previously demonstrated through AFM nanoindentation experiments (Fig. 5(a)) that erythrocytes exhibit rate-dependent mechanical responses, confirming their complex viscoelastic nature [41]. Specifically, increasing the indentation rate results in a higher reaction force Fig. 5(b), reflecting the role of dissipative processes alongside the elastic response of the spectrin network. In addition, erythrocyte stiffness is not spatially homogeneous, but reflects the intrinsic heterogeneity associated with their biconcave morphology. Comparative studies on healthy and pathological erythrocytes show that the latter tend to be stiffer, especially at intermediate indentation rates of 2–15 μm/s Fig. 5 (c), indicating a reduced ability of the cytoskeletal network to rearrange under stress. At higher rates, the difference narrows as both healthy and pathological erythrocytes reach a similar asymptotic stiffness, highlighting the dominance of elastic effects at those time scales.

Under physiological conditions, erythrocytes repeatedly undergo large and reversible deformations as they navigate narrow capillaries and interendothelial slits [42]. Their mechanical flexibility stems from the composite architecture of their membrane, which behaves as a polymer-like structure composed of a fluid phospholipid bilayer coupled to an underlying two-dimensional spectrin-actin cytoskeletal network [43]. The cytoskeleton forms a quasi-polymeric meshwork, imparting the membrane with shear elasticity and resilience against mechanical stress [44]. The lipid bilayer primarily governs bending rigidity and preserves membrane surface area, whereas the spectrin network — arranged in a hexagonal lattice cross-linked by short actin filaments — provides the primary in-plane elastic response. This hierarchical organization ensures the discoid shape, high deformability, and viscoelastic behavior that characterize healthy erythrocytes [45]. In various pathological conditions, such as diabetes mellitus, hypertension, arteriosclerosis, and coronary artery disease, the structural integrity and dynamic rearrangement of the cytoskeletal network are compromised [46]. Alterations in spectrin phosphorylation, oxidative damage, or changes in membrane lipid composition can stiffen the membrane, reducing its deformability and consequently increasing microvascular flow resistance [47].

To quantitatively describe the rate-dependent mechanical response of healthy and pathological erythrocytes, we fitted experimental data retrieved from Ref. [41] using Eq. (9). In these experiments, the indentation depth was set to 200 nm to minimize substrate effects. Pathological erythrocytes showed higher stiffness than healthy erythrocytes in the range 2–10 μm/s, whereas at larger indentation rates no significant changes are detected between healthy and pathological ones. Our model accounts for both the elastic and viscous responses of the erythrocyte membrane and cytoskeletal network, which together exhibit complex quasi-polymeric behavior under deformation. Generally, a higher effective viscosity typically correlates with a greater ability to dissipate energy and a more pronounced rate-dependent stiffening: Cells resist fast deformation and show higher forces at higher strain rates due to internal friction as observed in diabetic erythrocytes (Fig. 5(d) and

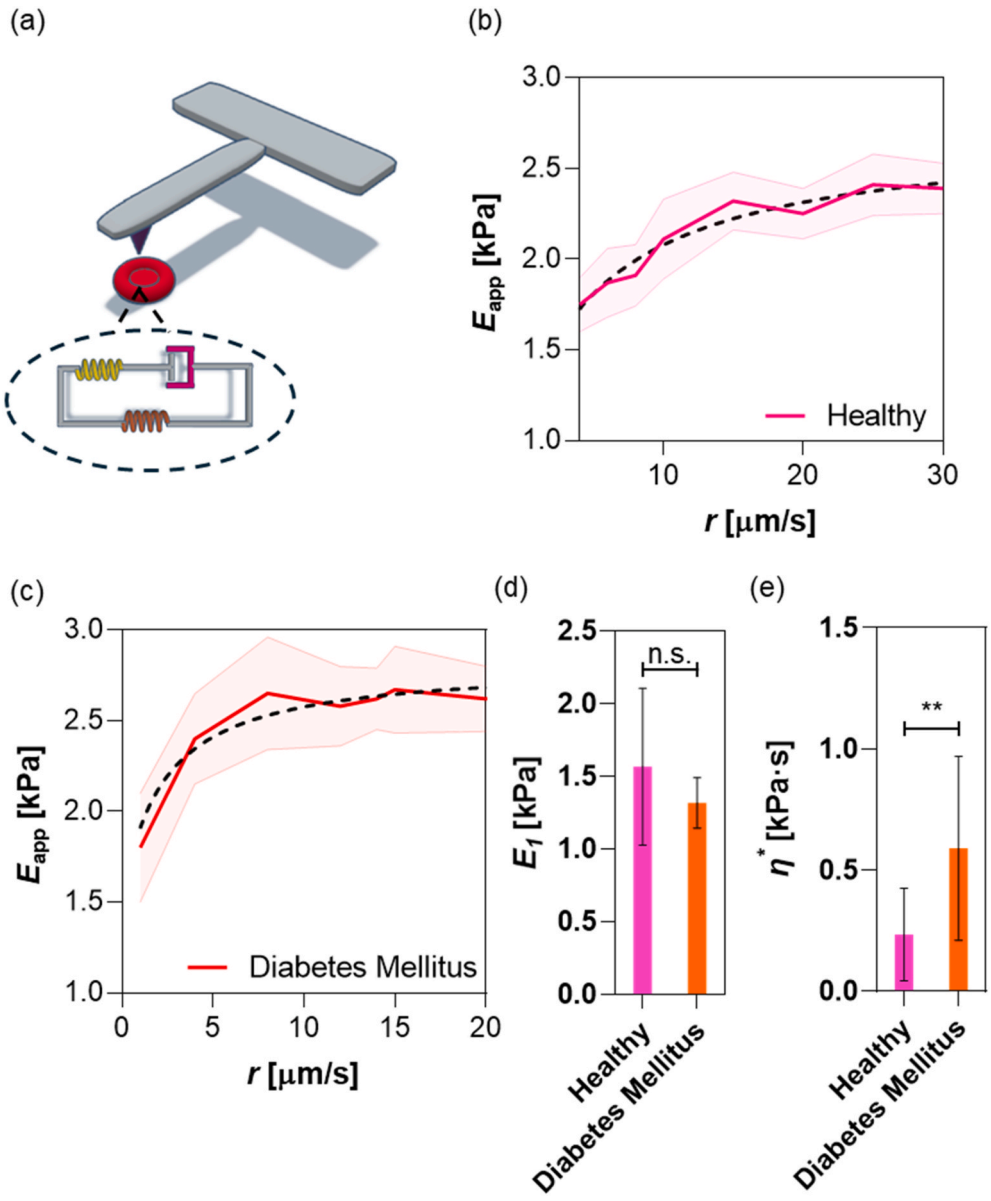

Fig. 5. (a) Sketch of AFM cantilever tip probing an erythrocyte. The inset shows the scheme of SLS model used to fit experimental data. Apparent Young's modulus of (b) healthy and (c) pathological erythrocytes as a function of indentation rate. The experimental data were retrieved from Ref. [41]. The solid lines represent the average Young's modulus, whereas the shaded areas the corresponding standard deviations. The data were fitted using Eq. (9) (dashed black lines). (d) Transient elastic moduli and (e) effective viscosities of healthy and pathological erythrocytes. Statistical significance was evaluated using unpaired *t*-test (not significant (n.s.) $p > 0.05$; $*p < 0.05$; $**p < 0.01$; $***p < 0.001$).

(e)), where increased membrane/cytoskeletal viscosity accompanies increased stiffness and loss of deformability [41]. In contrast, a lower effective viscosity implies a more elastic-dominated behavior – the material stores and releases mechanical energy more efficiently with minor loss, responding more immediately to stress. This is the case of healthy erythrocytes (Fig. 5(e)) that tend to be more compliant with faster stress relaxation, which can be advantageous for flexibility and resiliency [48].

3.3.2. *Porcine and equine zona pellucida*

The mechanical response of the zona pellucida (ZP) plays a crucial role in the mammalian fertilization process, including sperm binding and the prevention of polyspermy [49]. The ZP exhibits species-specific mechanical properties, which may contribute to differences in polyspermy rates and fertilization mechanisms across species. The composition of the ZP varies across species; for example, in mammals, it is primarily composed of sulfated glycoproteins that assemble into long fibrils, forming a three-dimensional extracellular network [50,51]. Understanding the mechanical behavior of ZP polymeric structure across different species is essential to elucidate its biological role in sperm–ZP interactions [52,53].

To better understand this mechanical response, we previously investigated the ZP of porcine and equine species using AFM nanoindentation [54]. Our findings demonstrated that the ZP acts as a viscoelastic polymer. Indeed, by increasing the indentation rate from 0.5 µm/s to 10 µm/s, we observed a comparable increase of the apparent elastic modulus for both species, approximately 5.3-fold for porcine (Fig. 6(a)) and 5-fold for equine (Fig. 6(b)), with an absolute value of the maximum apparent modulus significantly higher for porcine (160 kPa) compared to equine (15 kPa). Both the ZP tissues showed a linear dependance with indentation rate without approaching an asymptotic value up to 10 µm/s. This is coherent with typical penetration speeds of

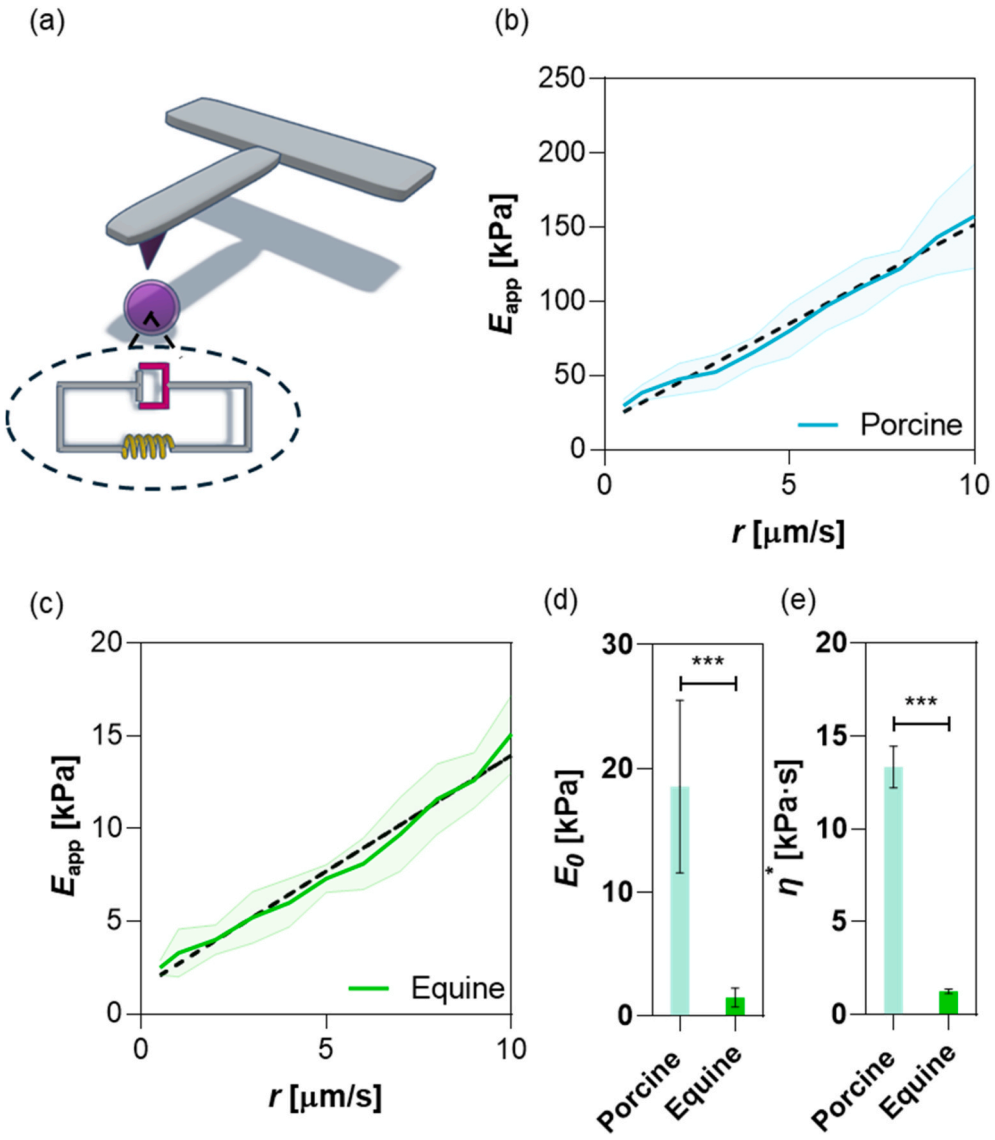

Fig. 6. (a) Sketch of AFM cantilever tip probing an oocyte. The inset shows the scheme of Kelvin-Voigt model used to fit experimental data. Apparent Young's modulus of (b) porcine and (c) equine zone pellucida as a function of indentation rate. The experimental data were retrieved from Ref. [54]. The solid lines represent the average Young's modulus, whereas the shaded areas the corresponding standard deviations. The data were fitted using Eq. (5) (dashed black lines). (d) Transient elastic moduli and (e) effective viscosities of porcine and equine zone pellucida. Statistical significance was evaluated using unpaired *t*-test (not significant (n.s.) $p > 0.05$; $^{*}p < 0.05$; $^{**}p < 0.01$; $^{***}p < 0.001$).

spermatozoa (25–50 µm/s) as an asymptotic value (at speeds lower than 10 µm/s) would have a negative impact on fertilization process due to the ZP hardening [55]. Therefore, to fit this curve we used Eq. (5) in which the elastic term is not predominant.

Notably, the apparent stiffness of porcine ZP is approximately 10 times higher than equine at the same indentation speeds, implying a stronger polymer network in porcine ZP (Fig. 6(a)–(c)). Yet both ZP types rely heavily on viscous damping: Papi et al. [54] found that viscous forces are predominant in the mechanical resistance of ZP. In other words, a significant portion of the force resisting indentation is due to time-dependent, dissipative processes (e.g., molecular rearrangements, fluid movement within the glycoprotein mesh), rather than purely elastic spring-back. The higher effective viscosity of the porcine ZP (consistent with its stiffer network) suggests it dissipates energy over longer timescales (Fig. 6(d)), which may help prevent sudden failure or cracking of the matrix under rapid loads (such as sperm impact). The equine ZP, while softer, still displays considerable viscous behavior (Fig. 6(d)) – its modulus rises with loading rate in parallel with porcine ZP.

4. Conclusions

The proposed approach offers several advantages: it is simple to implement using standard AFM datasets, requires no additional complex equipment or prolonged measurements, and delivers reliable estimates of the intrinsic elastic modulus while accounting for viscous contributions. These features make the method particularly suitable for rapid screening of soft biomaterials and biological structures, where time-dependent mechanical properties are critical for functionality. Typically, AFM-based stiffness measurements rely on quasi-static indentation speeds to minimize viscous effects, which makes the process time-consuming and limits throughput. In contrast, our method enables the characterization of material properties across a range of indentation rates, reducing acquisition time while still capturing both elastic and viscous behavior. Importantly, this approach facilitates the disentanglement of the material intrinsic stiffness from artifacts introduced by

the probing method—an essential step when designing constructs that aim to mimic the mechanical behavior of living tissues [56].

However, some limitations must be considered. Firstly, the approach assumes small deformations and ideal contact conditions, which may not fully represent the complex geometry or heterogeneity of biological samples. Secondly, the models used—while effective for the tested materials—are simplified representations that may not capture non-linearities or multiscale dynamics in highly heterogeneous or anisotropic systems. Thirdly, the ability to discriminate between the two viscoelastic models requires measurements at multiple indentation rates—at least three rates are needed to validate the apparent stiffness trend, especially for novel or poorly characterized biomaterials. In addition, accurate prediction still relies on high-quality AFM force curves, meaning that experimental variability or tip-sample adhesion can influence results. Finally, while effective in characterizing viscoelastic behavior, it remains unclear how cell–ECM interactions modulate the effective viscosity at the microscale, suggesting that further integration of biological complexity is needed to fully understand and replicate native tissue mechanics [31].

Future work should focus on refining the models to integrate poroelastic effects and structural anisotropy, as well as validating the method across a wider range of biological and engineered systems. Despite these challenges, this study provides a practical and robust framework for nanoscale biomechanical characterization, bridging a critical gap between complex rheological analyses and high-resolution AFM measurements. For instance, more complex biological systems, such as 3D cell-laden scaffolds and organoids, should be tested where multiscale heterogeneity and fluid interactions play a significant role. Incorporating poroelastic and nonlinear viscoelastic models could further improve accuracy. Additionally, coupling AFM with complementary techniques, such as optical or microrheology, may be useful to understand multiscale biomechanics and biomaterial hierarchical organization.

CRediT authorship contribution statement

Antonio Minopoli: Data curation, Formal analysis, Investigation, Methodology, Writing – original draft. **Davide Evangelista:** Data curation, Formal analysis, Investigation, Writing – original draft. **Matteo Marras:** Data curation, Formal analysis, Methodology, Writing – original draft. **Giordano Perini:** Formal analysis, Investigation, Validation, Writing – original draft. **Valentina Palmieri:** Formal analysis, Investigation, Project administration, Writing – original draft. **Marco De Spirito:** Conceptualization, Methodology, Project administration, Writing – original draft. **Massimiliano Papi:** Conceptualization, Methodology, Writing – original draft, Writing – review & editing.

Declaration of competing interest

The authors declare that they have no known competing financial interests or personal relationships that could have appeared to influence the work reported in this paper.

The author is an Editorial Board Member/Editor-in-Chief/Associate Editor/Guest Editor for this journal and was not involved in the editorial review or the decision to publish this article.

The authors declare the following financial interests/personal relationships which may be considered as potential competing interests.

Acknowledgments

This work was supported by the Italian Ministry of Health under the Ricerca Finalizzata POC 2023 program (Project Code PNRR-POC-2023-12377340).

We acknowledge the contribution of 3D Bioprinting Research Core Facility G-STeP of the Fondazione Policlinico Universitario A. Gemelli IRCCS for sample preparation and the G-STeP Microscopy Facility of the Fondazione Policlinico Universitario A. Gemelli IRCCS for atomic force microscopy experiments.

Data availability

Data will be made available on request.

References

[1] Y. Liu, Z. Li, J. Li, S. Yang, Y. Zhang, B. Yao, W. Song, X. Fu, S. Huang, Stiffness-mediated mesenchymal stem cell fate decision in 3D-bioprinted hydrogels, Burns Trauma 8 (2020) tkaa029, https://doi.org/10.1093/burnst/tkaa029.
[2] T. Xia, W. Liu, L. Yang, A review of gradient stiffness hydrogels used in tissue engineering and regenerative medicine, J. Biomed. Mater. Res. 105 (2017) 1799–1812, https://doi.org/10.1002/jbm.a.36034.
[3] F. Abasalizadeh, S.V. Moghaddam, E. Alizadeh, E. akbari, E. Kashani, S.M. B. Fazljou, M. Torbati, A. Akbarzadeh, Alginate-based hydrogels as drug delivery vehicles in cancer treatment and their applications in wound dressing and 3D bioprinting, J. Biol. Eng. 14 (2020) 8, https://doi.org/10.1186/s13036-020-0227-7.
[4] A. Minopoli, G. Perini, L. Cui, V. Palmieri, M. De Spirito, M. Papi, Biomaterial-driven 3D scaffolds for immune cell expansion toward personalized immunotherapy, Acta Biomater. 200 (2025) 132–157, https://doi.org/10.1016/j.actbio.2025.05.027.
[5] Y. Duan, X. Mi, Q. Yu, Z. Zhu, C. Gong, Y. Hong, H. Huang, S. He, L. Wang, Q. Guo, C. Zhu, B. Li, Tailored hydrogels for 3D bioprinting: matching tissue viscoelasticity to enhance resident cell functionality, Adv Funct Mater n/a (2025) 2503987, https://doi.org/10.1002/adfm.202503987.
[6] S.M. Hull, L.G. Brunel, S.C. Heilshorn, 3D bioprinting of cell-laden hydrogels for improved biological functionality, Adv. Mater. 34 (2022) 2103691, https://doi.org/10.1002/adma.202103691.
[7] F.J. Vernerey, S. Lalitha Sridhar, A. Muralidharan, S.J. Bryant, Mechanics of 3D cell–hydrogel interactions: experiments, models, and mechanisms, Chem. Rev. 121 (2021) 11085–11148, https://doi.org/10.1021/acs.chemrev.1c00046.
[8] M.D.A. Norman, S.A. Ferreira, G.M. Jowett, L. Bozec, E. Gentleman, Measuring the elastic modulus of soft culture surfaces and three-dimensional hydrogels using atomic force microscopy, Nat. Protoc. 16 (2021) 2418–2449, https://doi.org/10.1038/s41596-021-00495-4.
[9] A. Fischer-Cripps, D. Nicholson, Nanoindentation. Mechanical engineering series, Appl. Mech. Rev. 57 (2004), https://doi.org/10.1115/1.1704625. B12–B12.
[10] A. Yao, M. Tassieri, M. Padgett, J. Cooper, Microrheology with optical tweezers, Lab Chip 9 (2009) 2568, https://doi.org/10.1039/b907992k.
[11] M. Keller, J. Schilling, E. Sackmann, Oscillatory magnetic bead rheometer for complex fluid microrheometry, Rev. Sci. Instrum. 72 (2001) 3626–3634, https://doi.org/10.1063/1.1394185.
[12] C.A. Schuh, Nanoindentation studies of materials, Mater. Today 9 (2006) 32–40, https://doi.org/10.1016/S1369-7021(06)71495-X.
[13] N.K. Mukhopadhyay, P. Paufler, Micro- and nanoindentation techniques for mechanical characterisation of materials, Int. Mater. Rev. 51 (2006) 209–245, https://doi.org/10.1179/174328006X102475.
[14] G. Kerch, Polymer hydration and stiffness at biointerfaces and related cellular processes, Nanomedicine 14 (2018) 13–25, https://doi.org/10.1016/j.nano.2017.08.012.
[15] M.R. VanLandingham, J.S. Villarrubia, W.F. Guthrie, G.F. Meyers, Nanoindentation of polymers: an overview, Macromol. Symp. 167 (2001) 15–44, https://doi.org/10.1002/1521-3900(200103)167:1<15::AID-MASY15>3.0.CO;2-T.
[16] S.-V. Kontomaris, The hertz model in AFM nanoindentation experiments: applications in biological samples and biomaterials, Micro Nanosyst. 10 (2018) 11–22, https://doi.org/10.2174/1876402910666180426114700.
[17] O. Chaudhuri, Viscoelastic hydrogels for 3D cell culture, Biomater. Sci. 5 (2017) 1480–1490, https://doi.org/10.1039/C7BM00261K.
[18] C.-S. Han, S.H.R. Sanei, F. Alisafaei, On the origin of indentation size effects and depth dependent mechanical properties of elastic polymers, J. Polym. Eng. 36 (2016) 103–111, https://doi.org/10.1515/polyeng-2015-0030.
[19] Y.M. Efremov, W.-H. Wang, S.D. Hardy, R.L. Geahlen, A. Raman, Measuring nanoscale viscoelastic parameters of cells directly from AFM force-displacement curves, Sci. Rep. 7 (2017) 1541, https://doi.org/10.1038/s41598-017-01784-3.
[20] D.-L. Chen, P.-F. Yang, Y.-S. Lai, A review of three-dimensional viscoelastic models with an application to viscoelasticity characterization using nanoindentation, Microelectron. Reliab. 52 (2012) 541–558, https://doi.org/10.1016/j.microrel.2011.10.001.
[21] Y.M. Efremov, T. Okajima, A. Raman, Measuring viscoelasticity of soft biological samples using atomic force microscopy, Soft Matter 16 (2020) 64–81, https://doi.org/10.1039/C9SM01020C.
[22] S. Abuhattum, D. Mokbel, P. Müller, D. Soteriou, J. Guck, S. Aland, An explicit model to extract viscoelastic properties of cells from AFM force-indentation curves, iScience 25 (2022) 104016, https://doi.org/10.1016/j.isci.2022.104016.
[23] D. Tranchida, Z. Kiflie, S. Acierno, S. Piccarolo, Nanoscale mechanical characterization of polymers by atomic force microscopy (AFM) nanoindentations: viscoelastic characterization of a model material, Meas. Sci. Technol. 20 (2009) 095702, https://doi.org/10.1088/0957-0233/20/9/095702.

[24] P. Hajikarimi, F. Moghadas Nejad, Mechanical models of viscoelasticity, in: P. Hajikarimi, F. Moghadas Nejad (Eds.), Applications of Viscoelasticity, Elsevier, 2021, pp. 27–61, https://doi.org/10.1016/B978-0-12-821210-3.00003-6.
[25] C.-Y. Lin, Rethinking and researching the physical meaning of the standard linear solid model in viscoelasticity, Mech. Adv. Mater. Struct. 31 (2024) 2370–2385, https://doi.org/10.1080/15376494.2022.2156638.
[26] Z. El-Qoubaa, R. Othman, Characterization and modeling of the strain rate sensitivity of polyetheretherketone's compressive yield stress, Mater. Des. 66 (2015) 336–345, https://doi.org/10.1016/j.matdes.2014.10.080, 1980-2015.
[27] A.B. Kakarla, I. Kong, S.G. Nukala, W. Kong, Mechanical behaviour evaluation of porous scaffold for tissue-engineering applications using finite element analysis, J. Compos. Sci. 6 (2022) 46, https://doi.org/10.3390/jcs6020046.
[28] A.E. Chalard, H. Porritt, E.J. Lam Po Tang, A.J. Taberner, A. Winbo, A.M. Ahmad, J. Fitremann, J. Malmström, Dynamic composite hydrogels of gelatin methacryloyl (GelMA) with supramolecular fibers for tissue engineering applications, Biomater. Adv. 163 (2024) 213957, https://doi.org/10.1016/j.bioadv.2024.213957.
[29] V.B. Nguyen, C.X. Wang, C.R. Thomas, Z. Zhang, Mechanical properties of single alginate microspheres determined by microcompression and finite element modelling, Chem. Eng. Sci. 64 (2009) 821–829, https://doi.org/10.1016/j.ces.2008.10.050.
[30] S. Cai, Y. Hu, X. Zhao, Z. Suo, Poroelasticity of a covalently crosslinked alginate hydrogel under compression, J. Appl. Phys. 108 (2010) 113514, https://doi.org/10.1063/1.3517146.
[31] C. Huerta-López, A. Clemente-Manteca, D. Velázquez-Carreras, F.M. Espinosa, J. G. Sanchez, Á. Martínez-del-Pozo, M. García-García, S. Martín-Colomo, A. Rodríguez-Blanco, R. Esteban-González, F.M. Martín-Zamora, L.I. Gutierrez-Rus, R. Garcia, P. Roca-Cusachs, A. Elosegui-Artola, M.A. del Pozo, E. Herrero-Galán, P. Sáez, G.R. Plaza, J. Alegre-Cebollada, Cell response to extracellular matrix viscous energy dissipation outweighs high-rigidity sensing, Sci. Adv. 10 (2024) eadf9758, https://doi.org/10.1126/sciadv.adf9758.
[32] A. Brzyska, W. Płaziński, Modeling conformational changes in alginic acid oligomers induced by external forces, Carbohydr. Res. 545 (2024) 109294, https://doi.org/10.1016/j.carres.2024.109294.
[33] T. Ramdhan, S.H. Ching, S. Prakash, B. Bhandari, Physical and mechanical properties of alginate based composite gels, Trends Food Sci. Technol. 106 (2020) 150–159, https://doi.org/10.1016/j.tifs.2020.10.002.
[34] J. Zhang, H. Yang, B.E. Abali, M. Li, Y. Xia, R. Haag, Dynamic mechanics-modulated hydrogels to regulate the differentiation of stem-cell spheroids in soft microniches and modeling of the nonlinear behavior, Small 15 (2019) 1901920, https://doi.org/10.1002/smll.201901920.
[35] H. Li, X. Lian, D. Guan, Crossover behavior in stress relaxations of poroelastic and viscoelastic dominant hydrogels, Soft Matter 19 (2023) 5443–5451, https://doi.org/10.1039/D3SM00592E.
[36] W. Deng, Y. Tang, J. Mao, Y. Zhou, T. Chen, X. Zhu, Cellulose nanofibril as a crosslinker to reinforce the sodium alginate/chitosan hydrogels, Int. J. Biol. Macromol. 189 (2021) 890–899, https://doi.org/10.1016/j.ijbiomac.2021.08.172.
[37] A.A. Aldana, F. Valente, R. Dilley, B. Doyle, Development of 3D bioprinted GelMA-alginate hydrogels with tunable mechanical properties, Bioprinting 21 (2021) e00105, https://doi.org/10.1016/j.bprint.2020.e00105.
[38] M.N. Moghadam, D.P. Pioletti, Improving hydrogels' toughness by increasing the dissipative properties of their network, J. Mech. Behav. Biomed. Mater. 41 (2015) 161–167, https://doi.org/10.1016/j.jmbbm.2014.10.010.
[39] H. Li, X. Lian, D. Guan, Crossover behavior in stress relaxations of poroelastic and viscoelastic dominant hydrogels, Soft Matter 19 (2023) 5443–5451, https://doi.org/10.1039/D3SM00592E.
[40] O. Chaudhuri, Viscoelastic hydrogels for 3D cell culture, Biomater. Sci. 5 (2017) 1480–1490, https://doi.org/10.1039/C7BM00261K.
[41] G. Ciasca, M. Papi, S. Di Claudio, M. Chiarpotto, V. Palmieri, G. Maulucci, G. Nocca, C. Rossi, M. De Spirito, Mapping viscoelastic properties of healthy and pathological red blood cells at the nanoscale level, Nanoscale 7 (2015) 17030–17037, https://doi.org/10.1039/C5NR03145A.
[42] M. Dao, I. MacDonald, R.J. Asaro, Erythrocyte flow through the interendothelial slits of the splenic venous sinus, Biomech. Model. Mechanobiol. 20 (2021) 2227–2245, https://doi.org/10.1007/s10237-021-01503-y.
[43] M. Dao, C.T. Lim, S. Suresh, Mechanics of the human red blood cell deformed by optical tweezers, J. Mech. Phys. Solid. 51 (2003) 2259–2280, https://doi.org/10.1016/j.jmps.2003.09.019.
[44] D.E. Discher, P. Carl, New insights into red cell network structure, elasticity, and spectrin unfolding-a current review, Cell. Mol. Biol. Lett. 6 (2001) 593–606.
[45] M. Puig-de-Morales-Marinkovic, K.T. Turner, J.P. Butler, J.J. Fredberg, S. Suresh, Viscoelasticity of the human red blood cell, Am. J. Physiol. Cell Physiol. 293 (2007) C597–C605, https://doi.org/10.1152/ajpcell.00562.2006.
[46] S. Hareendranath, S.P. Sathian, Dynamic response of red blood cells in health and disease, Soft Matter 19 (2023) 1219–1230, https://doi.org/10.1039/D2SM01090A.
[47] J.L. Maciaszek, G. Lykotrafitis, Sickle cell trait human erythrocytes are significantly stiffer than normal, J. Biomech. 44 (2011) 657–661, https://doi.org/10.1016/j.jbiomech.2010.11.008.
[48] D.E. McMillan, N.G. Utterback, T.P. Mitchell, Doublet formation of diabetic erythrocytes as a model of impaired membrane viscous deformation, Microvasc. Res. 26 (1983) 205–220, https://doi.org/10.1016/0026-2862(83)90071-7.
[49] P. Coy, S. Cánovas, I. Mondéjar, M.D. Saavedra, R. Romar, L. Grullón, C. Matás, M. Avilés, Oviduct-specific glycoprotein and heparin modulate sperm–zona pellucida interaction during fertilization and contribute to the control of polyspermy, Proc. Natl. Acad. Sci. 105 (2008) 15809–15814, https://doi.org/10.1073/pnas.0804422105.
[50] D.P.L. Green, Three-dimensional structure of the zona pellucida, Rev. Reprod. 2 (1997) 147–156.
[51] P.M. Wassarman, Zona pellucida glycoproteins, Annu. Rev. Biochem. 57 (1988) 415–442, https://doi.org/10.1146/annurev.bi.57.070188.002215.
[52] E. Priel, T. Priel, I. Szaingurten-Solodkin, T. Wainstock, Y. Perets, A. Zeadna, A. Harlev, E. Lunenfeld, E. Levitas, I. Har-Vardi, Zona pellucida shear modulus, a possible novel non-invasive method to assist in embryo selection during in-vitro fertilization treatment, Sci. Rep. 10 (2020) 14066, https://doi.org/10.1038/s41598-020-70739-y.
[53] P.M. Wassarman, E.S. Litscher, Female fertility and the zona pellucida, eLife 11 (2022) e76106, https://doi.org/10.7554/eLife.76106.
[54] M. Papi, A. Maiorana, C. Douet, G. Maulucci, T. Parasassi, R. Brunelli, G. Goudet, M. De Spirito, Viscous forces are predominant in the zona pellucida mechanical resistance, Appl. Phys. Lett. 102 (2013) 043703, https://doi.org/10.1063/1.4789503.
[55] A. Boccaccio, M.C. Frassanito, L. Lamberti, R. Brunelli, G. Maulucci, M. Monaci, M. Papi, C. Pappalettere, T. Parasassi, L. Sylla, F. Ursini, M. De Spirito, Nanoscale characterization of the biomechanical hardening of Bovine zona pellucida, J. R. Soc. Interface 9 (2012) 2871–2882, https://doi.org/10.1098/rsif.2012.0269.
[56] C.F. Guimarães, L. Gasperini, A.P. Marques, R.L. Reis, The stiffness of living tissues and its implications for tissue engineering, Nat. Rev. Mater. 5 (2020) 351–370, https://doi.org/10.1038/s41578-019-0169-1.